CONFIDENTIAL

Copy 261
RM L54H31

NACA RM L54H31

NACA

RESEARCH MEMORANDUM

A SUMMARY OF THE LOW-LIFT DRAG AND LONGITUDINAL TRIM CHARACTERISTICS OF TWO VERSIONS OF AN INTERCEPTOR-TYPE AIRPLANE AS DETERMINED FROM FLIGHT TESTS OF ROCKET-POWERED MODELS AT MACH NUMBERS BETWEEN 0.75 AND 1.78

By Willard S. Blanchard, Jr.

Langley Aeronautical Laboratory
Langley Field, Va.

CLASSIFICATION CHANGED TO UNCLASSIFIED
AUTHORITY: NASA TECHNICAL PUBLICATIONS ANNOUNCEMENTS NO. 11
EFFECTIVE DATE: DECEMBER 1, 1959 WHL

CLASSIFIED DOCUMENT

This material contains information affecting the National Defense of the United States within the meaning of the espionage laws, Title 18, U.S.C., Secs. 793 and 794, the transmission or revelation of which in any manner to an unauthorized person is prohibited by law.

NATIONAL ADVISORY COMMITTEE FOR AERONAUTICS

WASHINGTON

November 26, 1954

CONFIDENTIAL

NATIONAL ADVISORY COMMITTEE FOR AERONAUTICS

RESEARCH MEMORANDUM

A SUMMARY OF THE LOW-LIFT DRAG AND LONGITUDINAL TRIM CHARACTERISTICS OF TWO VERSIONS OF AN INTERCEPTOR-TYPE AIRPLANE AS DETERMINED FROM FLIGHT TESTS OF ROCKET-POWERED MODELS AT MACH NUMBERS BETWEEN 0.75 AND 1.78

By Willard S. Blanchard, Jr.

SUMMARY

Low-lift drag and longitudinal trim data are presented herein for two versions of an interceptor-type airplane, the second of which had a slimmer nose and a thinner tail than the first. The data were obtained from free-flight tests of rocket-powered models at Mach numbers between 0.75 and 1.78, and Reynolds numbers between about 5×10^6 and 15×10^6, respectively (based on mean aerodynamic chord). Data are presented for three models (complete, wingless, and horizontal tailless) of the first version, and from one model (complete configuration) of the second version.

For both versions tested, the low-lift longitudinal trim change was mild. For the complete model of the first version the external drag coefficient varied from 0.012 at subsonic speeds to about 0.043 at supersonic speeds. For the complete model of the second version, the external drag coefficient was about the same as that of the first version at subsonic speeds, but was 0.0035 lower at $M = 1.20$, and 0.0080 lower at $M = 1.70$. The drag rise for the complete models of both versions began at $M = 0.93$.

Both the complete and the horizontal-tailless models of the first version exhibited mild wing flutter at Mach numbers between about 0.95 and 1.10. The wing, however, did not structurally duplicate the airplane wing. The second version, which had a stiffer wing, exhibited no indications of flutter, and none of the models reported herein exhibited any indication of buffet during these tests.

INTRODUCTION

The Langley Pilotless Aircraft Research Division has conducted rocket-powered free-flight tests of models of two versions of an interceptor-type airplane configuration. The primary purpose of these tests was to ascertain the drag and longitudinal trim characteristics at low lift. In addition, however, some longitudinal stability and pitch-damping data were obtained.

The basic configuration was conventional in general geometry, and consisted of a swept wing mounted low on a nose-inlet-type fuselage. For the purpose of the tests reported herein, however, the nose inlet was faired to a point ahead of the proposed inlet location. The horizontal tail was mounted slightly below the center line of the fuselage base. The modified version differed from the original in that the canopy was smaller, the nose fairing was slimmer, and the horizontal tail, in addition to being mounted lower on the fuselage, was only half as thick, as was the vertical tail. Complete models of both versions were tested; in addition, a wingless model and a horizontal-tailless model of the first version were tested.

SYMBOLS

M	free-stream Mach number
R	Reynolds number based on mean aerodynamic chord
W	model weight, lb
$\bar{c}$	mean aerodynamic chord, 1.245 ft
S	model wing area (leading and trailing edges extended to fuselage center line), 4.56 sq ft
C_C	chord force coefficient, $\frac{\text{Chord force}}{qS}$
C_D	drag coefficient, $\frac{\text{Drag}}{qS}$
ΔC_D	pressure-drag coefficient
dC_D/dM	rate of change of drag coefficient with Mach number

C_N normal-force coefficient, $\frac{\text{Normal force}}{qS}$

C_L lift coefficient, $\frac{\text{Lift}}{qS}$

C_m pitching-moment coefficient about the center of gravity, $\frac{\text{Pitching moment}}{qS\bar{c}}$

C_{m_o} pitching-moment coefficient at zero lift

C_{m_α} rate of change of pitching-moment coefficient with angle of attack, $\partial C_m/\partial\alpha$, per deg

P period of the short-period longitudinal oscillation, sec

θ angle between model reference line and the horizontal, deg

$q = \frac{1}{57.3}\frac{d\theta}{dt}$, radians/sec, or dynamic pressure, lb/sq ft

$\dot{\alpha} = \frac{1}{57.3}\frac{d\alpha}{dt}$, radians/sec

C_{L_α} rate of change of lift coefficient with angle of attack, $dC_L/d\alpha$, per deg

V velocity, ft/sec

t time, sec

γ flight-path angle, degrees above horizontal

$C_{m_q} = \frac{\partial C_m}{\partial\frac{q\bar{c}}{2V}}$, per radian

$C_{m_{\dot{\alpha}}} = \frac{\partial C_m}{\partial\frac{\dot{\alpha}\bar{c}}{2V}}$, per radian

A cross-sectional area or aspect ratio

l	model length, nose to fuselage base, in.
x	distance measured rearward from nose, in.
r	radius, in.
a_l/g	longitudinal-accelerometer reading
a_n/g	normal-accelerometer reading
$T_{1/2}$	time required for the short-period longitudinal oscillation to damp to one-half amplitude, sec
p_o	free-stream static pressure, lb/sq in.
p_{base}	fuselage base pressure, lb/sq in.

MODELS

Figures 1(a) and 1(b) are three-view drawings of the complete models of the first and second version, respectively. Figures 2(a) and 2(b) show cross-sectional areas of the components of both versions plotted nondimensionally against fuselage station. Figure 3 shows total cross-sectional area of both versions plotted dimensionally against fuselage station for direct comparison. Figures 4 to 7 are photographs of the models, and table I includes geometric dimensions of the models of both versions.

As stated previously, the models had no duct inlet; the fuselage lines were faired to a point ahead of the proposed inlet location. Each fuselage was built around a $5\frac{1}{2}$-inch-diameter steel tube which served to house the sustainer rocket motor and to secure the nose, wing, and tail. Each fuselage was of mahogany with the exception of the nose, which was of fiber glass with a heat-resistant plastic used as a bonding agent, and the extreme afterbody, which was an aluminum casting. The sustainer motors were solid-fuel rockets developing about 3,700 pounds thrust for 1 second.

Each model was equipped with two small rocket motors which were used to disturb the model in pitch at preset times during flight. These pulse rockets may be seen in figure 5.

The wings and the horizontal and vertical tails were swept 45° at the quarter chord on both versions of the model tested, and were mounted at zero incidence with respect to the model center lines. The wingless

model was equipped with a 45°-swept, 3-percent-thick stabilizing ventral fin of double-wedge section, as described in reference 1, in order to establish lateral stability.

On the three models tested of the first version, the wings and tails were of mahogany construction with aluminum spars. On the model of the second version tested, the wing was solid aluminum, and the horizontal and vertical tails were solid steel.

For each of the models tested, instrumentation consisted of a four-channel telemeter. In the complete and horizontal-tailless models of the first version, quantities measured were free-stream total pressure, normal acceleration, longitudinal acceleration, and fuselage base pressure. In the wingless model, a horizontal-tail vibrometer was substituted for the fuselage base pressure. In the complete model of the second version, a horizontal-tail normal accelerometer was substituted for the fuselage base pressure.

TEST PROCEDURE

The models were boosted to about $M = 1.30$ (except the wingless model, which was boosted to about $M = 1.80$) by solid-fuel Deacon rocket motors developing about 6,000 pounds average thrust for 3 seconds. The sustainer motors accelerated the models from about $M = 1.30$ to about $M = 1.80$, except the wingless model, which had no sustainer motor. Throughout the flights, continuous records of all quantities measured were recorded by two independent ground receiving stations. The models were tracked in flight by two radar sets, one recording position in space and the other recording velocity.

A radiosonde was released immediately following each flight, and transmitted continuous records of atmospheric density, pressure, and temperature throughout the altitude ranges traversed by the model flights. The radiosonde balloons were tracked by a radar set and position data obtained thereby were utilized to determine wind velocity and direction throughout the altitude ranges of the tests.

METHOD OF ANALYSIS

All data reported herein were obtained from the decelerating portions of the flights where the models were separated from the boosters and the sustainer rocket motors were not thrusting. Dynamic pressure and Mach number were determined from telemetered total pressure, radar velocity data, and radiosonde data.

Drag

Total drag was determined by two independent methods. The first consisted of differentiation with respect to time of the velocity (as determined from radar tracking, and corrected for line-of-sight) and calculation of total-drag coefficient by the relationship

$$C_{D_{total}} = -\left(\frac{dV}{dt} + 32.2 \sin \gamma\right)\frac{W}{32.2qS}$$

where q was based on velocity from radar, corrected for line of sight and for winds.

The second method consisted of calculation of the total-drag coefficient by the relationship

$$C_{D_{total}} = C_C = -\frac{a_l}{g}\frac{W}{qS}$$

where a_l/g was determined directly from telemetered data and $C_{D_{total}}$ was assumed equal to C_C since the model flew near zero lift.

External drag was calculated from the relationship

$$C_D = C_{D_{total}} - C_{D_{base}} - C_{D_{stabilizing\ fin}}$$

where

$$C_{D_{base}} = \frac{A_{base}}{S}\frac{P_o - P_{base}}{q}$$

and where P_{base} was measured on the complete and horizontal tailless models of the first version, and where $C_{D_{stabilizing\ fin}}$ (applicable only to the wingless model) was determined from reference 1.

Lift

Lift was determined from the relationship

$$C_L = C_N = \frac{a_n}{g} \frac{W}{qS}$$

where a_n/g was obtained from telemetered data, and C_L was assumed equal to C_N since the models flew near zero lift.

Static longitudinal stability and pitch damping were determined by the methods used in reference 2.

Accuracy

Mach number measurements are felt to be accurate within ±0.02; drag coefficient within ±0.0010; lift coefficient within ±0.0030. The figures quoted are maximum probable values, and in general the errors are appreciably smaller than the quoted values.

DISCUSSION OF RESULTS

Reynolds number for the tests reported herein varied from about 5×10^6 at $M = 0.75$ to about 15×10^6 at $M = 1.78$, as shown in figure 8. For the complete, wingless, and horizontal-tailless models of the first version, the center of gravity was located 19.6, 16.7, and 8.8 percent, respectively, behind the leading edge of the mean aerodynamic chord. For the second version (complete model), the center of gravity was 20.6 percent behind the leading edge of the mean aerodynamic chord. Mass moments of inertia in pitch were 7.42, 4.47, and 6.75 slug-feet^2 for the complete, wingless, and horizontal-tailless models of the first version, and 8.40 slug-feet^2 for the complete model of the second version.

Longitudinal Trim

Figures 9 and 10 present data from the present tests showing the variation of the trim lift coefficient with Mach number for the first and second versions tested. In figure 10, trim lift coefficient is shown for the complete models of both versions in order to facilitate direct comparison. For both versions the low-lift trim lift coefficient indicates with increasing Mach number a trim change consisting of a moderate

nosing-up tendency between $M = 0.90$ and $M = 1.00$, a gentle nosing-up tendency between $M = 1.00$ and $M = 1.30$, and a gentle nosing-down tendency from $M = 1.30$ to the highest Mach numbers tested. It should be noted that at larger tail deflections, the shape of the trim change may vary drastically due to changes in control effectiveness and stability with Mach number. It is interesting to note that throughout the tested Mach number range, an increment of about 0.04 exists between the trim lift coefficients for the two versions (complete models). The center-of-gravity location was approximately the same for these two models (19.6 percent mean aerodynamic chord for the first and 20.6 percent for the second version, as noted previously). This increment in trim-lift coefficient is probably caused partially by the vertical location of the horizontal tail. For the second version, the horizontal tail was located near the bottom of the fuselage, and hence was probably affected by upwash around the bottom of the convergent afterbody; the first version had its horizontal tail located near the center line of the afterbody. Another probable factor is the difference in body nose shape between the first and second versions.

Shown in figure 9, in addition to data from the present tests, are unpublished trim data for complete and horizontal-tailless sting-mounted models of the first version, as obtained in wind-tunnel tests. Agreement between the test reported herein and these tunnel data is fair at the lower Mach numbers, and good at the higher speeds, as can be seen in figure 11. The tunnel-tested models were smaller than the models of the test reported herein.

Drag

Total drag and chord-force coefficients are shown in figure 11 for all three models of the first version. The data for the model with no horizontal tail (shown faired by dashed line) are felt to be questionable quantitatively because of an apparent longitudinal accelerometer shift, and are presented primarily to give a qualitative indication of drag increment caused by the horizontal tail. Figure 12 shows base drag which is applicable to all three models of the first version, and stabilizing ventral-fin drag, which is applicable only to the wingless model. Figure 13 shows drag coefficient for all three models of the first version as obtained from the present tests, and in addition unpublished data obtained from wind-tunnel tests of comparable models are also shown. Agreement between the present tests and the tunnel data is fair. The present tests indicate that at subsonic speeds, increments of drag coefficient caused by either the wing or horizontal tail are about 0.0030; at supersonic speeds, the increments are about 0.0070 for the horizontal tail, and about 0.0130 for the wing.

Shown in figure 14 are total-drag and chord-force coefficients for the complete model of the second version. Base drag is shown in figure 15. Figure 16 shows drag coefficient for this model and for the complete model of the first version, in order to facilitate direct comparison. As can be seen in figure 16, both models have a subsonic drag level of about 0.0120. The drag rise for both models, based on $dC_D/dM = 0.10$, begins at $M = 0.93$. At $M = 1.20$, the drag of the second version is 0.0395 as compared to 0.043 for the first version. At $M = 1.70$, the values are 0.035 and 0.043, respectively. Thus the increment in drag coefficient indicates that the second version has 0.0035 less drag at $M = 1.20$, and 0.0080 less drag at $M = 1.70$. The increment of 0.0035 at $M = 1.20$ is substantiated by figure 17(a), which shows both calculated and measured pressure drag for the complete models of both versions. Figure 17(a) shows that while the method presented in reference 3 for calculating pressure drag does not yield a true indication of the magnitude of the pressure drag for an airplane of this type, it does predict the increment caused by small changes, such as those existing between the first and second versions reported herein. This occurrence is also noted in reference 4. As shown in figure 17, agreement between the increment from the present tests and the increment from calculated values is excellent at $M = 1.20$. Also shown in figure 17(a) is pressure drag measured (see ref. 4) on a tested body of revolution having area distribution equivalent to that of the first version reported herein. Agreement between the body-of-revolution model and the calculated pressure drag is fair at $M = 1.20$; the calculated value is low by a factor of about 15 percent. Indications similar to those discussed above (i.e., that the method of ref. 3 will predict changes in pressure drag brought about by relatively small changes in area distribution) have been observed on other similar (swept-wing) configurations. It is interesting to note, however, that in the case of the tests reported herein, the increment of pressure drag between the complete models of the first and second versions at $M = 1.20$ can also be attributed directly to the difference in the thickness of the tail surfaces of the two versions. The horizontal and vertical tails were 7 percent thick on the first version, and $3\frac{1}{2}$ percent thick on the second version.

Figure 17(b) shows calculated and measured pressure drag of the complete and wingless models of the first version, along with unpublished data for the wing alone, obtained from rocket-model tests of wings mounted on slim "spike" bodies. As can be seen in figure 17(b), calculations (by the method of ref. 3) do not predict the pressure drag of either the complete model or the wingless model. However, it should be noted that the pressure drag is more nearly predicted for the wingless model than for the complete model. It is also shown in figure 17(b) that there is apparently some favorable interference effect between the wing and body, since the measured increment of pressure drag between the complete model and the wingless model is appreciably less than the measured pressure drag of the wing alone.

Longitudinal Stability

Shown in figure 18 is the period of the short-period pitch oscillation of the four models tested. Figure 19 shows the longitudinal stability parameter C_{m_α} for the models tested. Shown in figure 20 is the estimated lift-curve slope for each of the models. These values of lift-curve slope are based on wind-tunnel tests of rigid models of the first version, corrected by the method of reference 5 for the flexibility of the models in this test. As can be seen in figure 20, the lift-curve slope for the complete model of the second version is somewhat higher than that for the complete model of the first version. This is a result of the greater flexibility of the wings and tails of the first version as compared to the second - a result of the different types of construction employed, as discussed on previous pages.

Shown in figure 21 is aerodynamic-center location for the models tested, based on C_{m_α} from figure 19 and C_{L_α} from figure 20. Also included in figure 21 are tunnel data from complete models of the first version for comparison. Comparison of the data from the complete models of the first and second versions shows that the second version has its aerodynamic center located farther aft than that of the first version. This is felt to be due largely to the stiffer tail (solid steel) on the second version.

Figure 22 shows time required for the short-period pitch oscillation to damp to 1/2 amplitude. These values were used along with the values of lift-curve slope shown in figure 20 to calculate the pitch-damping parameter, $C_{m_q} + C_{m_{\dot{\alpha}}}$, shown in figure 23. Also shown in figure 23 is damping calculated for both of the complete models by the method of reference 6, using estimated downwash obtained from reference 7. As shown in figure 23, damping from the tests reported herein is lower than the calculated values at the lower supersonic speeds tested, and higher at the higher speeds, than the calculated values.

Figure 24 shows C_{m_0} for the complete models of both versions as obtained using figures 10 and 21. As can be seen in figure 24, C_{m_0} does not show rapid change with Mach number over any portion of the flights for which these data were obtained. Between $M = 1.25$ and $M = 1.72$, the values are about 0.02 higher for the first version than for the second.

Flutter and Buffet

Both the complete and the horizontal-tailless models of the first version exhibited indications of mild wing flutter at Mach numbers between

about 0.95 and 1.10 at a frequency of 50 cycles per second. First- and second-bending frequencies of the wings of these models were about 30 and 100 cycles per second. The amplitude of the oscillation was about 0.3g in both cases, as measured by the normal accelerometer which was located 5 inches outboard of the fuselage center line at about midchord. The other models tested (the wingless model of the first version, and the complete model of the second version) exhibited no indication of flutter. First- and second-bending frequencies of the wing of the second version were 55 and 190 cycles per second.

None of the models reported herein exhibited any indication of buffet during these tests, which were at low lift coefficients.

CONCLUSIONS

From the flight tests at low lift of rocket-powered models of two versions (the second of which had a slimmer nose and a thinner tail) of an interceptor-type airplane at Mach numbers between 0.75 and 1.78 and Reynolds numbers between about 5×10^6 and 15×10^6, respectively (based on mean aerodynamic chord), the following conclusions are indicated:

1. For both versions, the longitudinal trim change was mild.

2. For the complete model of the first version, the external drag coefficient varied from 0.012 at $M = 0.80$ to about 0.043 at supersonic speeds.

3. The external drag coefficient for the complete model of the second version was about the same as that of the first version at subsonic speeds, but was 0.0035 lower at $M = 1.20$, and 0.0080 lower at $M = 1.70$.

4. For the complete models of both versions, the drag rise, based on $dC_D/dM = 0.10$, began at $M = 0.93$.

5. Both the complete and the horizontal-tailless models of the first version exhibited mild wing flutter at Mach numbers between about 0.95 and 1.10. The complete model of the second version, which had a stiffer wing, exhibited no indications of flutter.

6. There was no indication of buffet during any portion of the tests reported herein.

Langley Aeronautical Laboratory,
National Advisory Committee for Aeronautics,
Langley Field, Va., August 25, 1954.

REFERENCES

1. Stoney, William E., Jr.: Pressure Distributions at Mach Numbers From 0.6 to 1.9 Measured in Free Flight on a Parabolic Body of Revolution With Sharply Convergent Afterbody. NACA RM L51L03, 1952.

2. Gillis, Clarence L., Peck, Robert F., and Vitale, A. James: Preliminary Results From a Free-Flight Investigation at Transonic and Supersonic Speeds of the Longitudinal Stability and Control Characteristics of an Airplane Configuration With a Thin Straight Wing of Aspect Ratio 3. NACA RM L9K25a, 1950.

3. Nelson, Robert L., and Stoney, William E., Jr.: Pressure Drag of Bodies at Mach Numbers up to 2.0. NACA RM L53I22c, 1953.

4. Hall, James Rudyard: Comparison of Free-Flight Measurements of the Zero-Lift Drag Rise of Six Airplane Configurations and Their Equivalent Bodies of Revolution at Transonic Speeds. NACA RM L53J21a, 1954.

5. Vitale, A. James: Effects of Wing Elasticity on the Aerodynamic Characteristics of an Airplane Configuration Having 45° Sweptback Wings As Obtained From Free-Flight Rocket-Model Tests at Transonic Speeds. NACA RM L52L30, 1953.

6. Gillis, Clarence L., and Chapman, Rowe, Jr.: Summary of Pitch-Damping Derivatives of Complete Airplane and Missile Configurations As Measured in Flight at Transonic and Supersonic Speeds. NACA RM L52K20, 1953.

7. Weil, Joseph, Campbell, George S., and Diederich, Margaret S.: An Analysis of Estimated and Experimental Transonic Downwash Characteristics As Affected by Plan Form and Thickness for Wing and Wing-Fuselage Configurations. NACA RM L52I22, 1952.

TABLE I.- GEOMETRIC DIMENSIONS

	First version	Second version
Wing:		
Total area, sq ft	4.56	4.56
Exposed area, sq ft	3.54	3.54
Aspect ratio	3.56	3.56
Sweepback (quarter chord), deg	45	45
Taper ratio	0.30	0.30
Horizontal tail:		
Total area, sq ft	1.20	1.20
Exposed area, sq ft	0.85	0.85
Aspect ratio	3.56	3.56
Sweepback (quarter chord), deg	45	45
Taper ratio	0.30	0.30
Dihedral, deg	2.00	0
Vertical tail:		
Total area (to center line), sq ft . .	0.60	0.69
Exposed area, sq ft	0.46	0.54
Aspect ratio	1.76	1.45
Sweepback (quarter chord), deg	45	45
Taper ratio	0.28	0.41
Fuselage:		
Frontal area, sq ft	0.32	0.32
Length, ft	*5.25	*5.47
Base area, sq ft	0.054	0.084
Fuselage nose to wing leading edge (center line), ft	*1.725	*1.90
Fuselage nose to horizontal-tail leading edge (center line), ft	*4.135	*4.14
Wing chord plane to fuselage reference line, ft	0.104	0.104
Tail chord plane to fuselage reference line, ft	0.058	0.161
Wing airfoil section, free stream . . .	NACA 64A007	NACA 64A007
Horizontal- and vertical-tail airfoil sections, free stream	NACA 64A007	NACA 64A003.5

*Includes faired nose (no inlet).

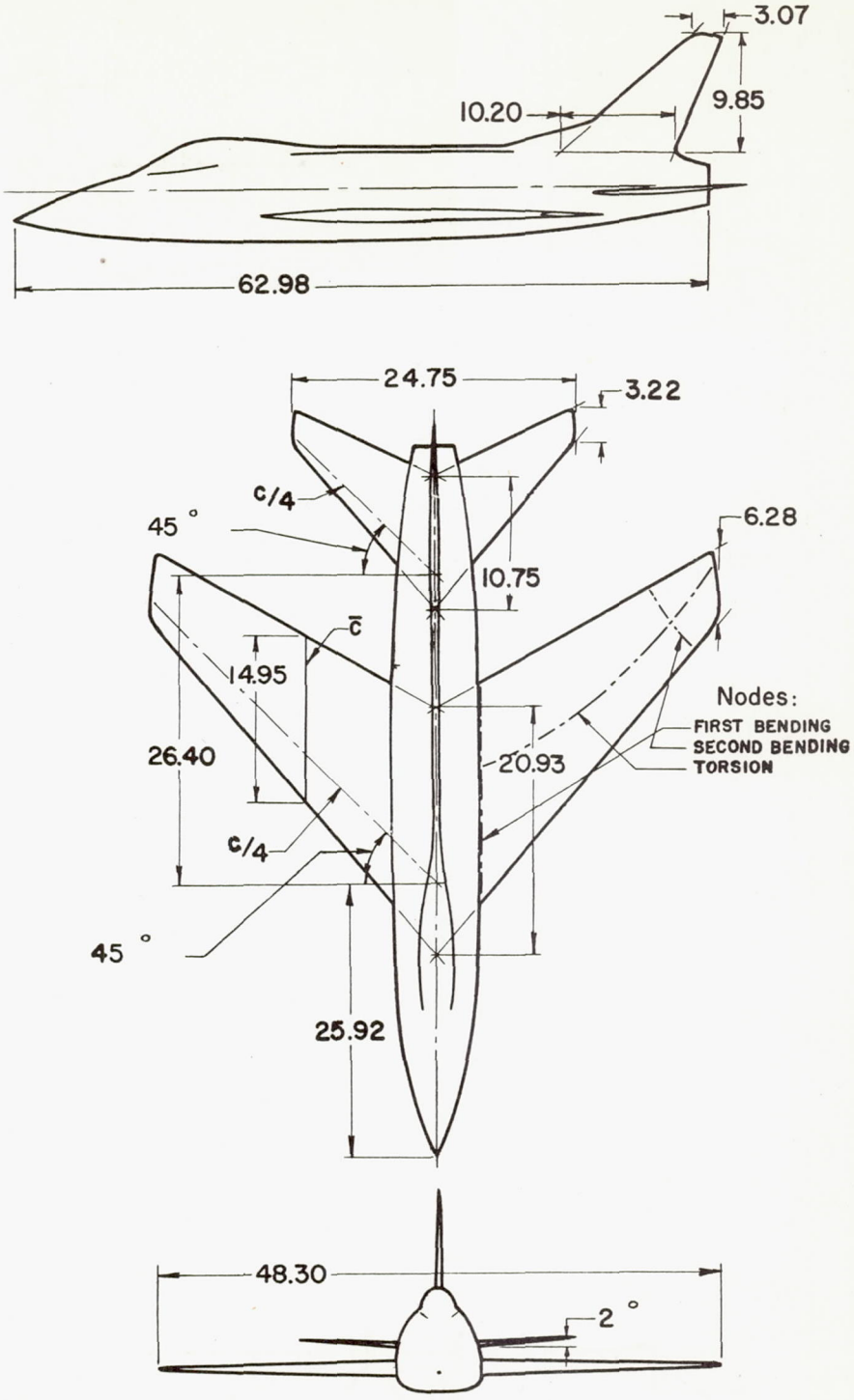

(a) Complete model of the first version.

Figure 1.- Three-view drawings. All dimensions are in inches unless otherwise noted.

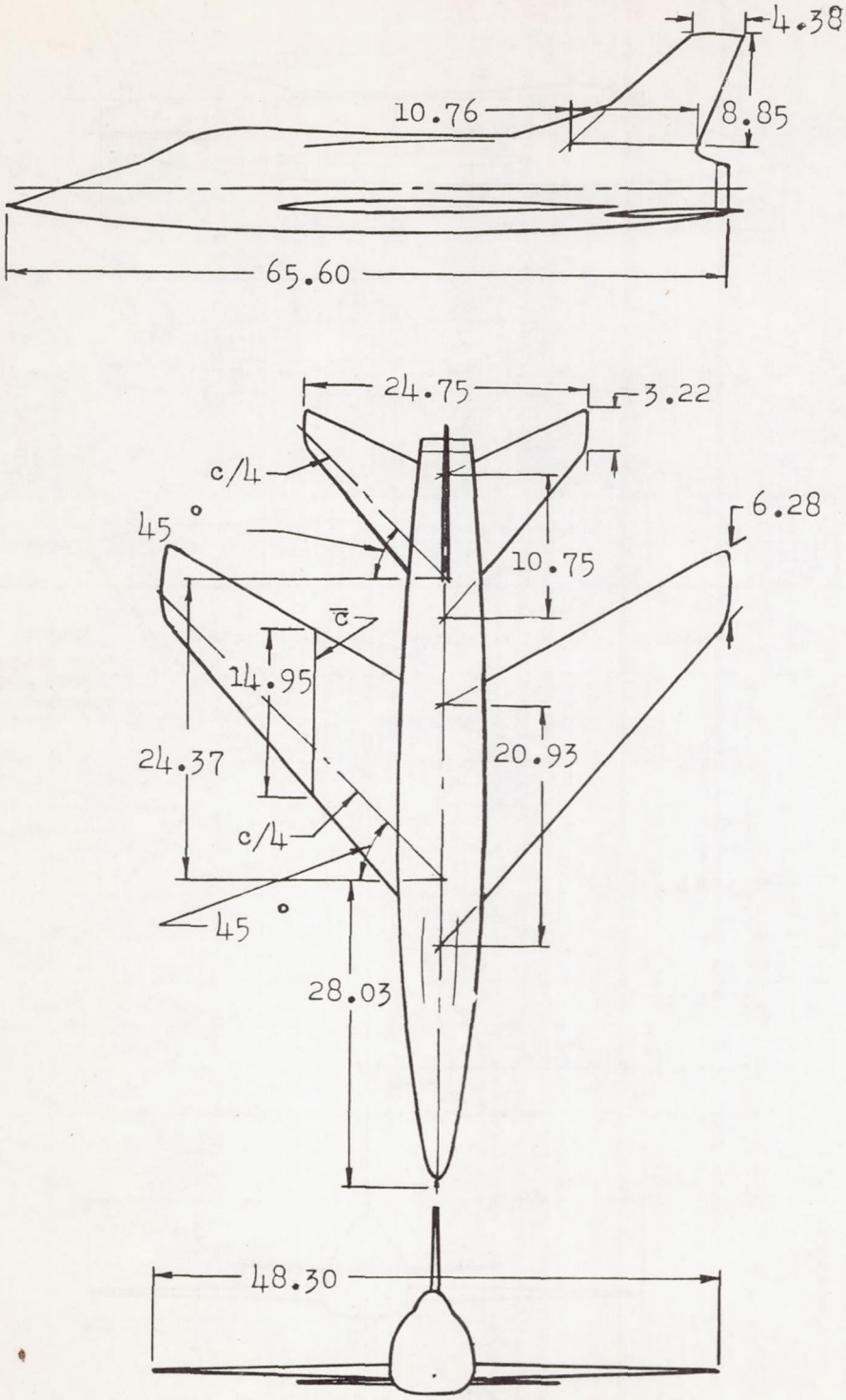

(b) The second version.

Figure 1.- Concluded.

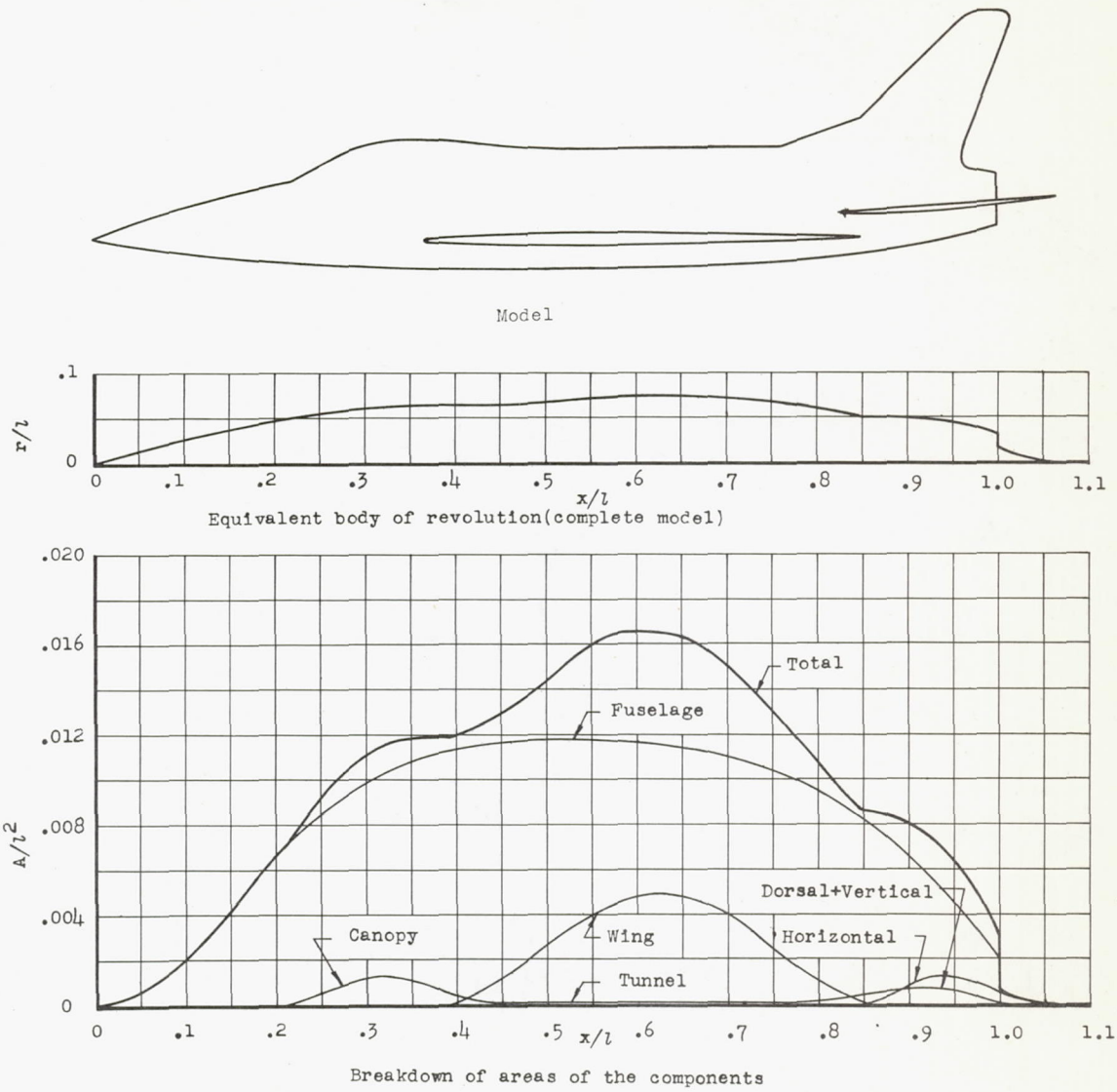

(a) The first version.

Figure 2.- Nondimensional area distribution.

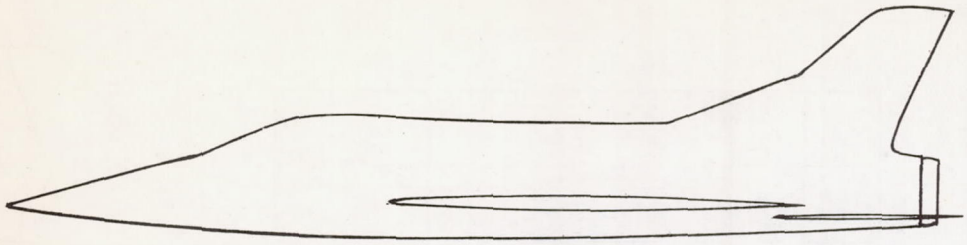

Model

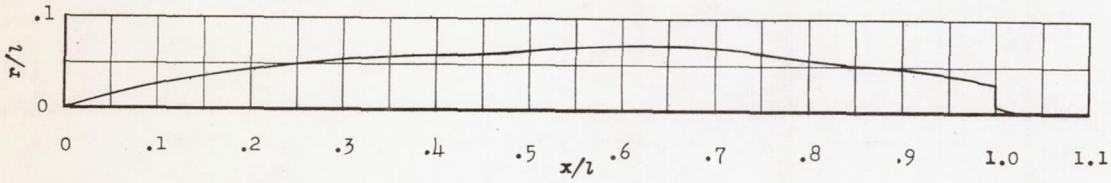

Equivalent body of revolution(complete model).

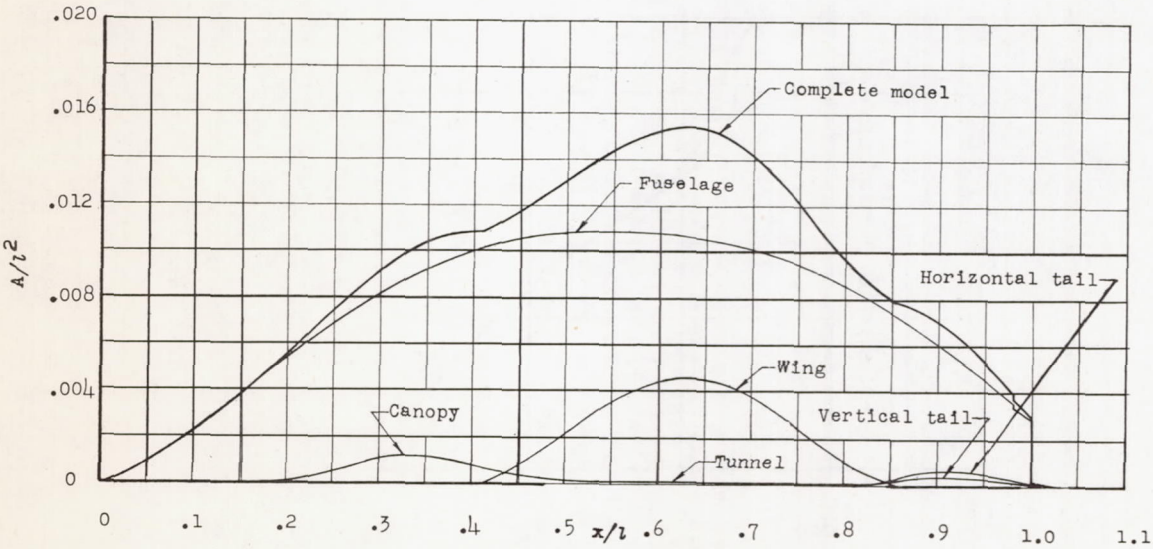

Breakdown of areas of the components.

(b) The second version.

Figure 2.- Concluded.

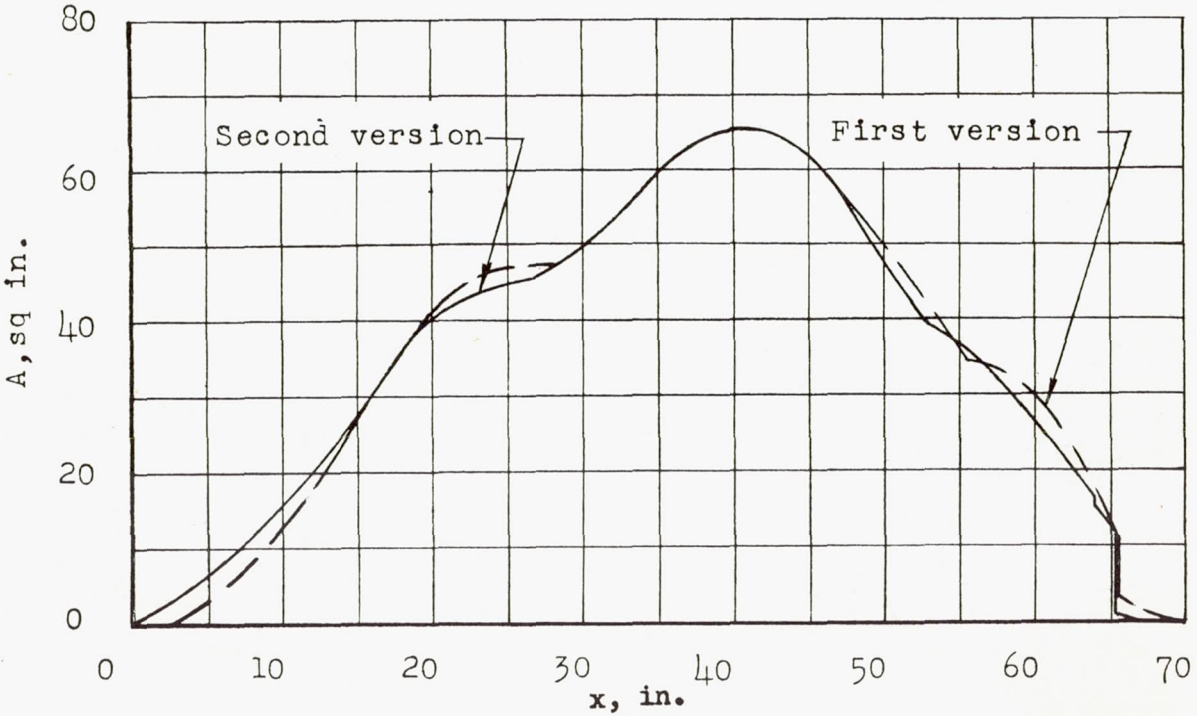

Figure 3.- Dimensional area distribution of the complete models of both versions; zero station is that of the second version.

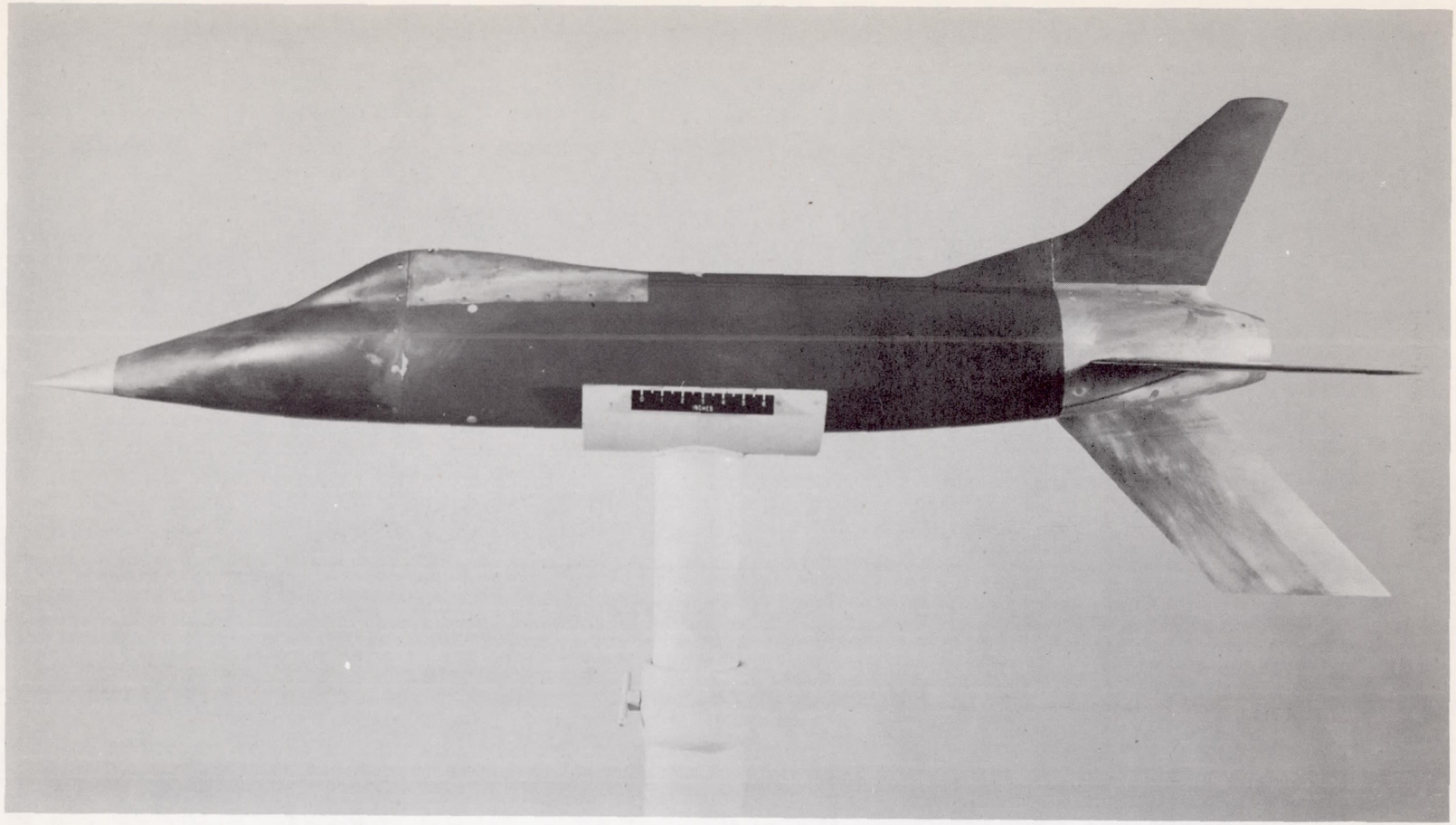

L-80004

Figure 4.- Photograph of the wingless model of the first version showing the stabilizing ventral fin.

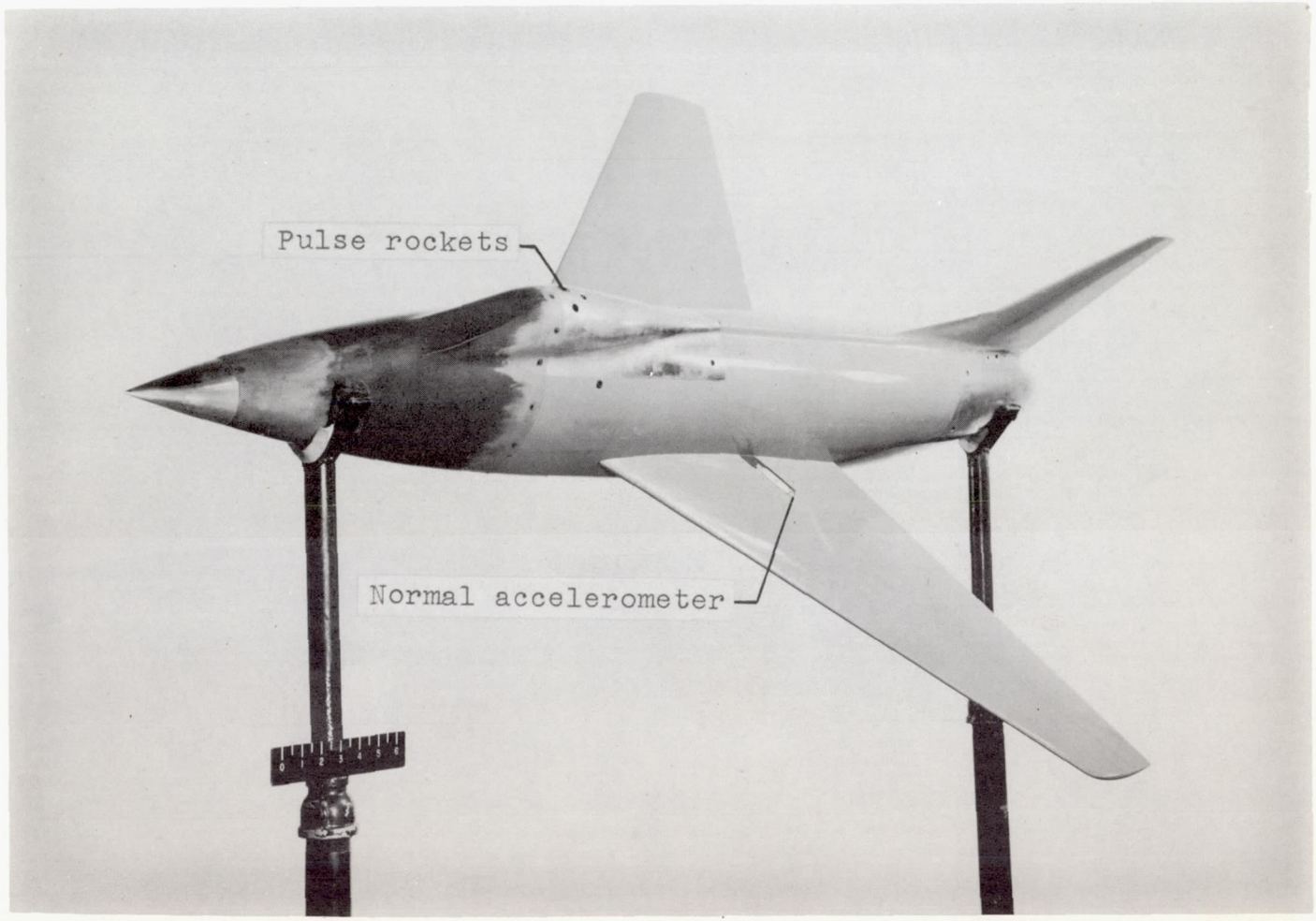

L-79023.1

Figure 5.- The horizontal-tailless model of the first version.

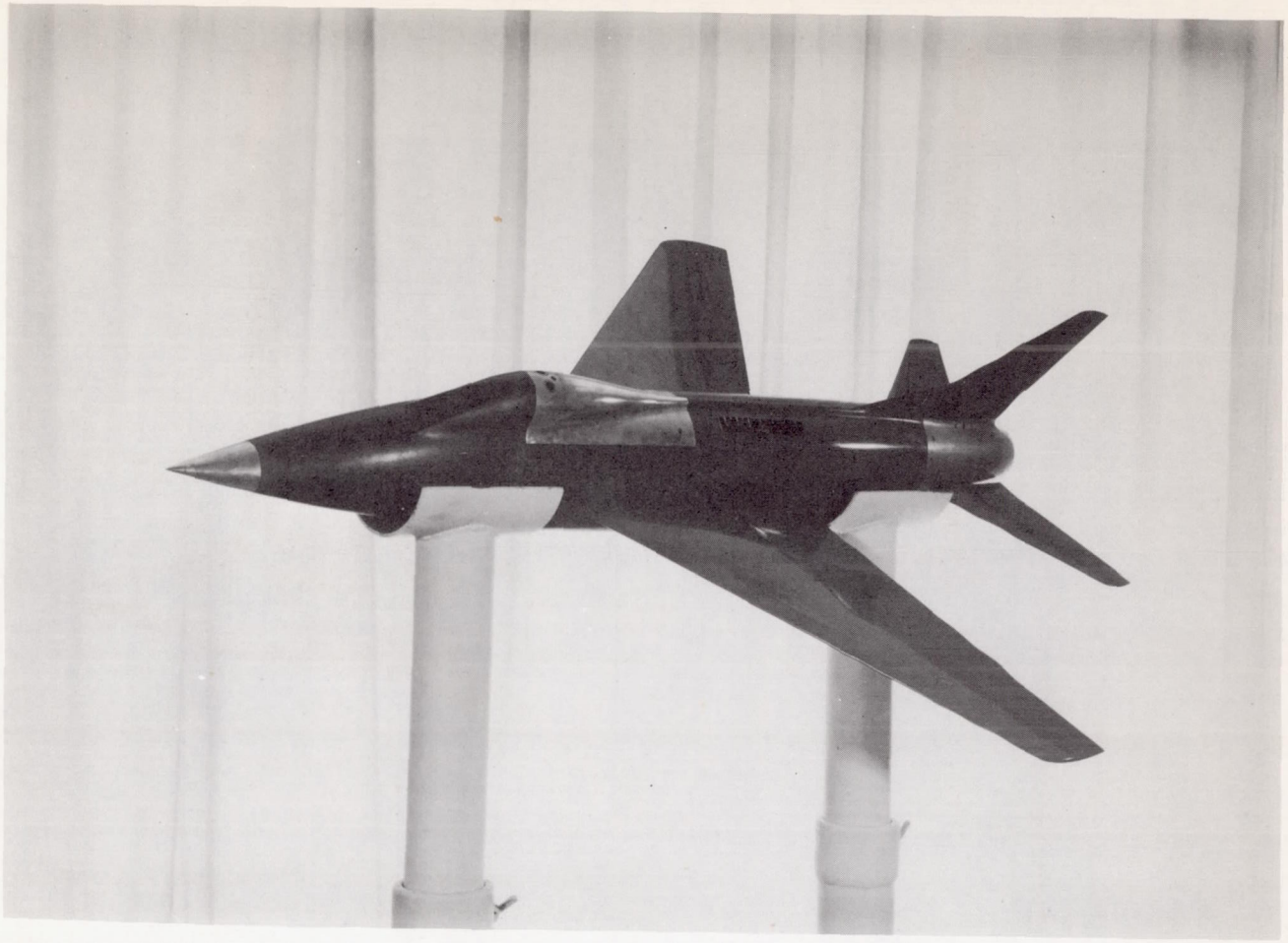

L-77767

Figure 6.- Three-quarter front view of the complete model of the first version.

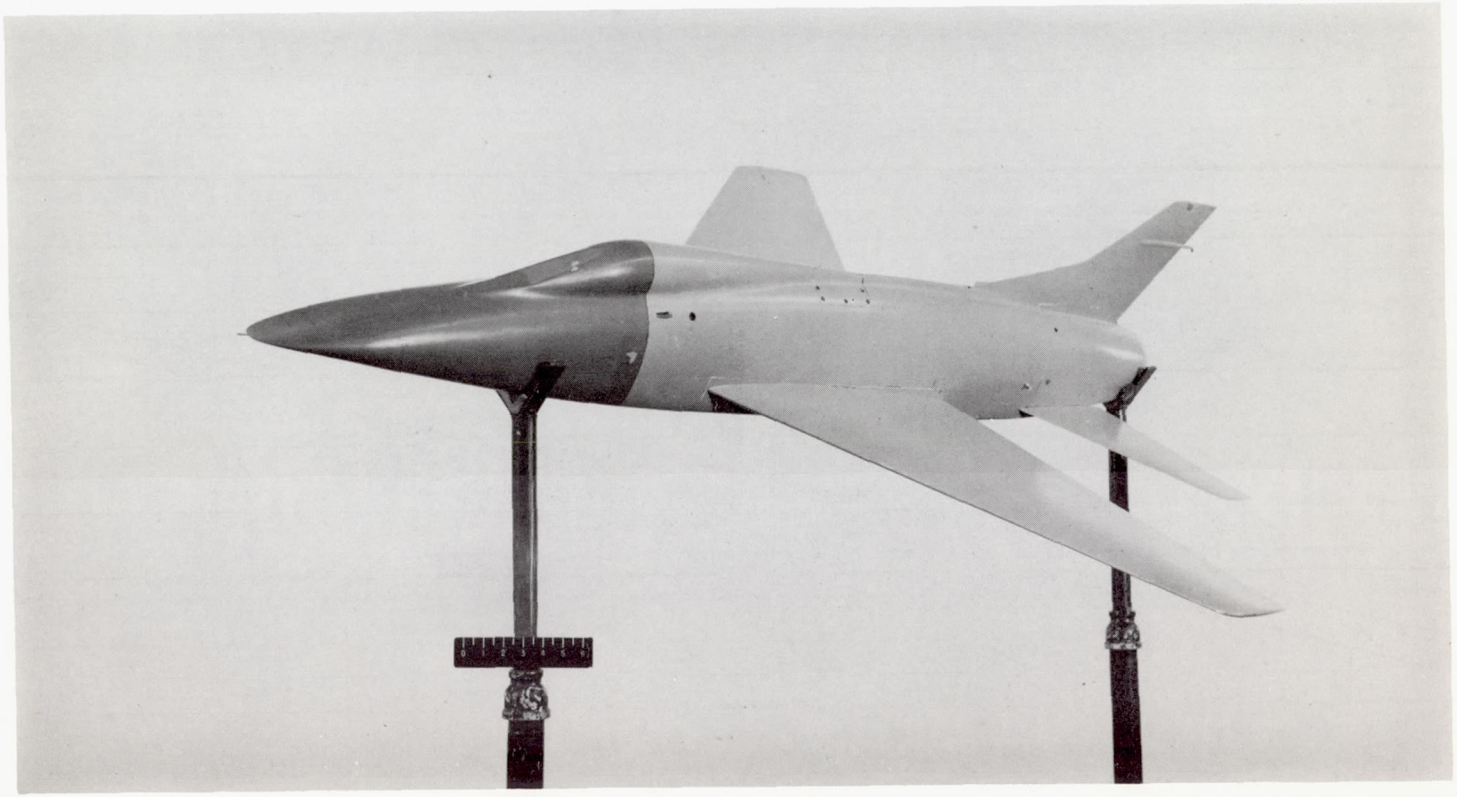

L-80907.1

Figure 7.- Three-quarter front view of the second version (complete model).

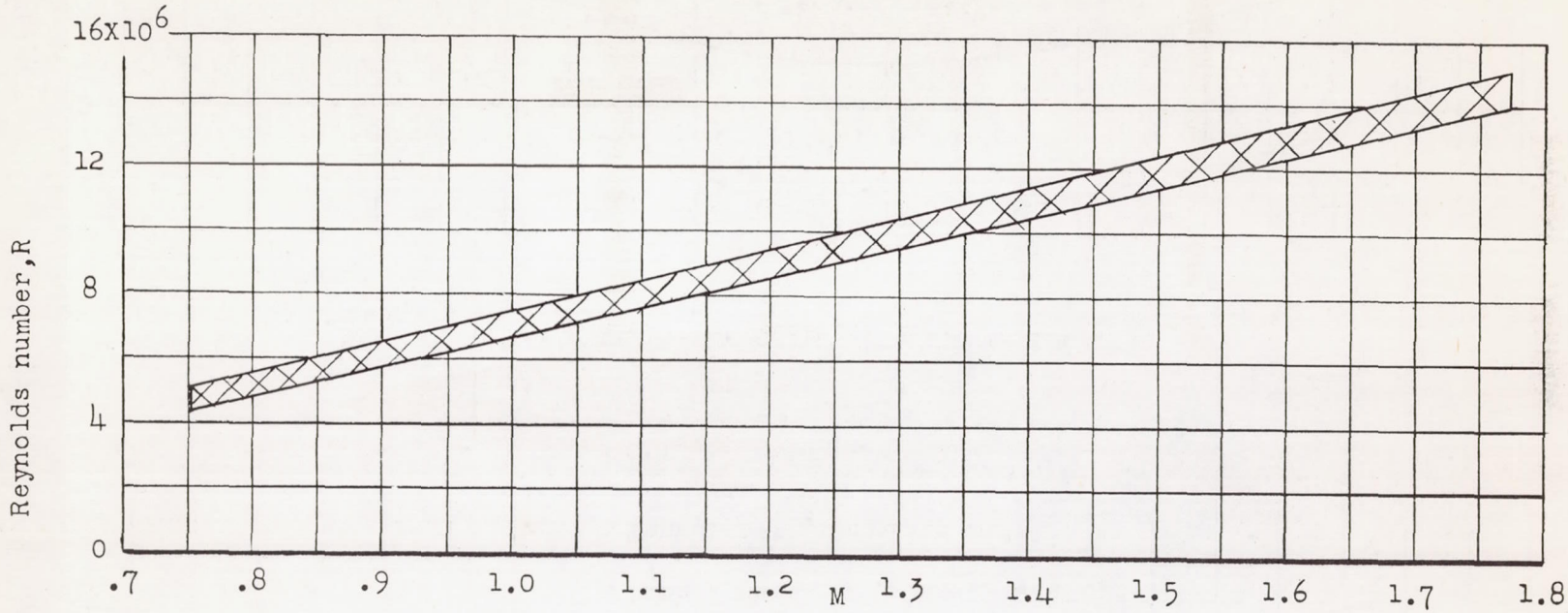

Figure 8.- Variation of Reynolds number with Mach number.

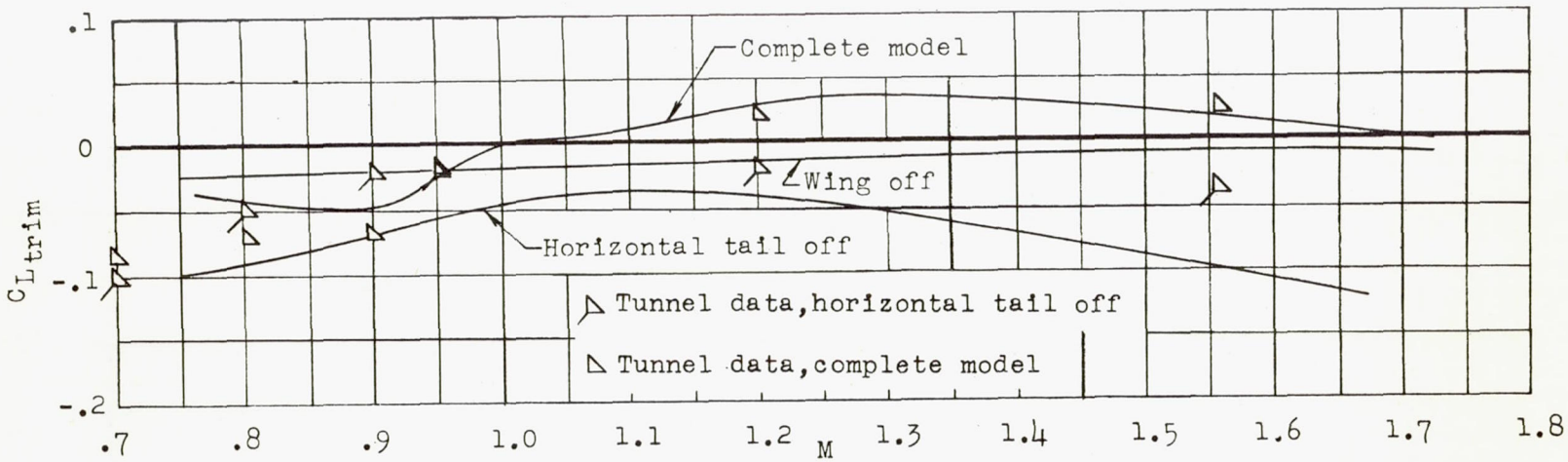

Figure 9.- Trim lift (first version).

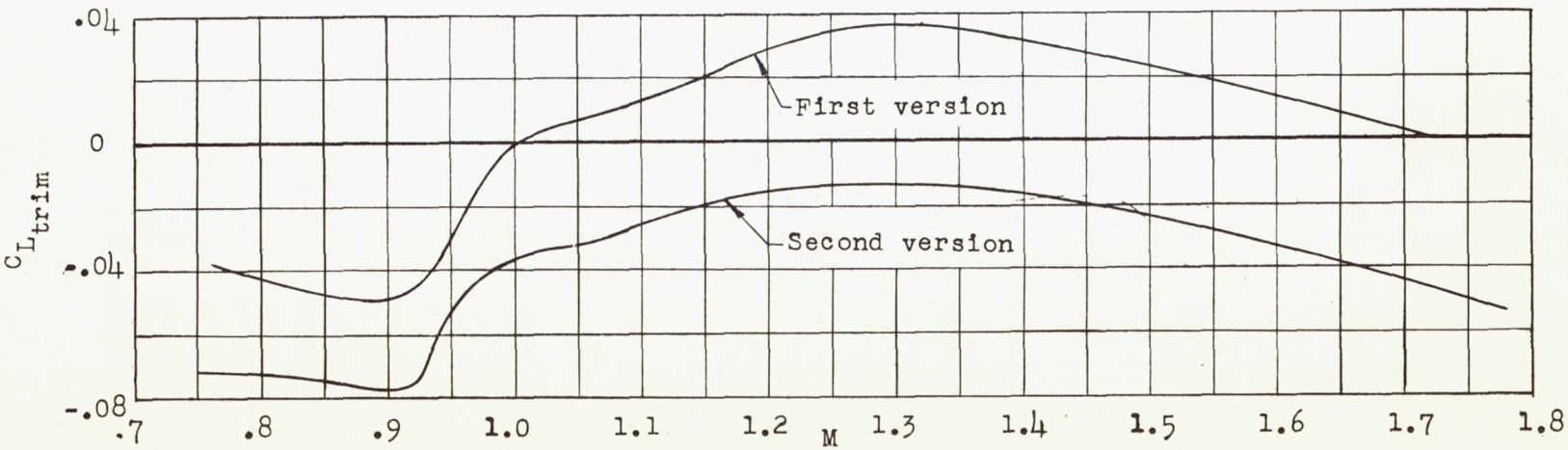

Figure 10.- Trim lift (complete models of both versions).

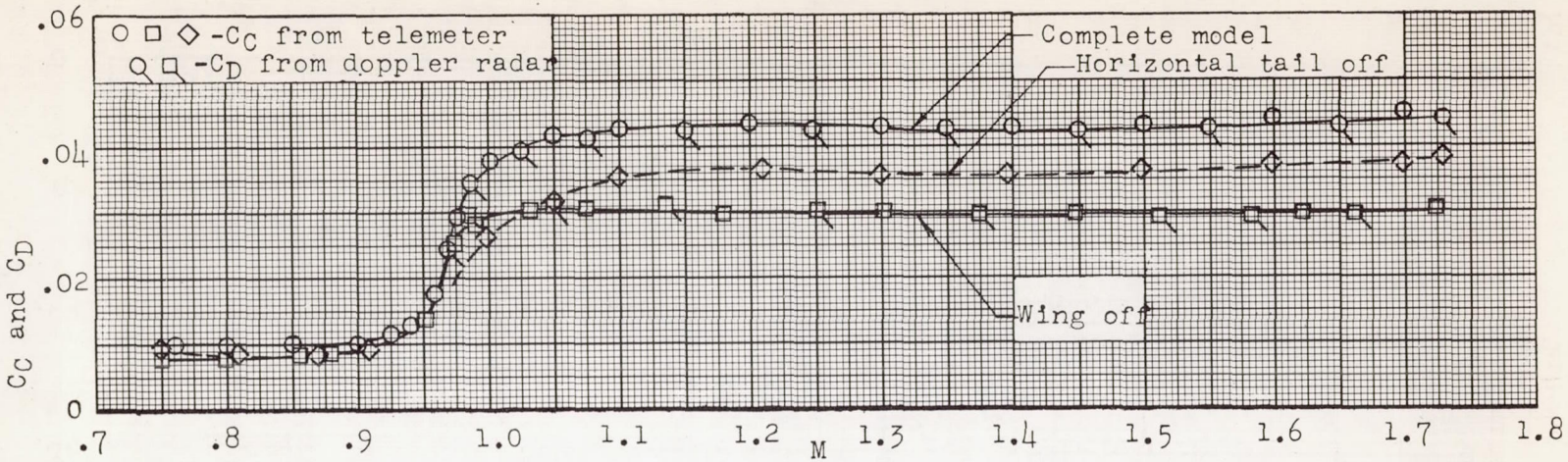

Figure 11.- Total drag and chord force (first version).

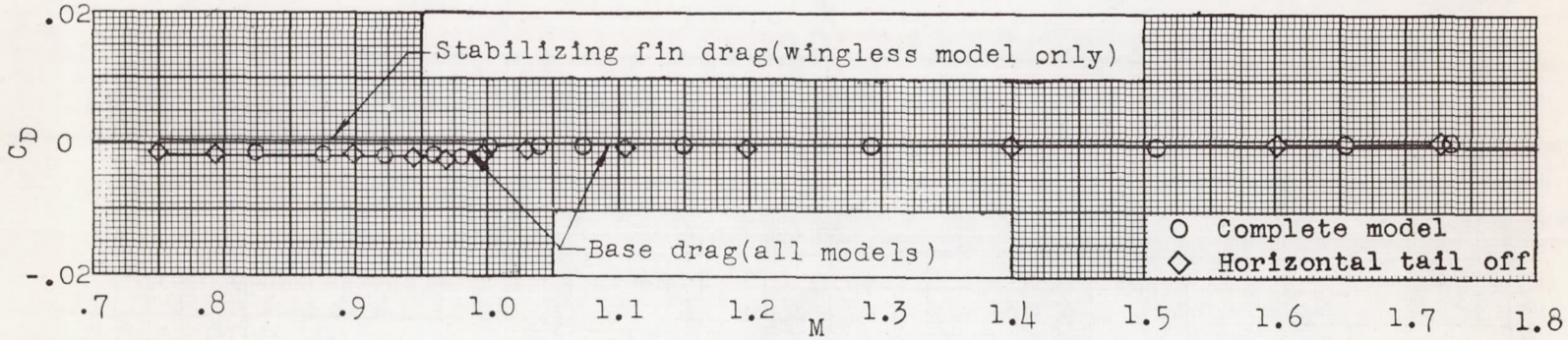

Figure 12.- Base drag and stabilizing-fin drag (first version).

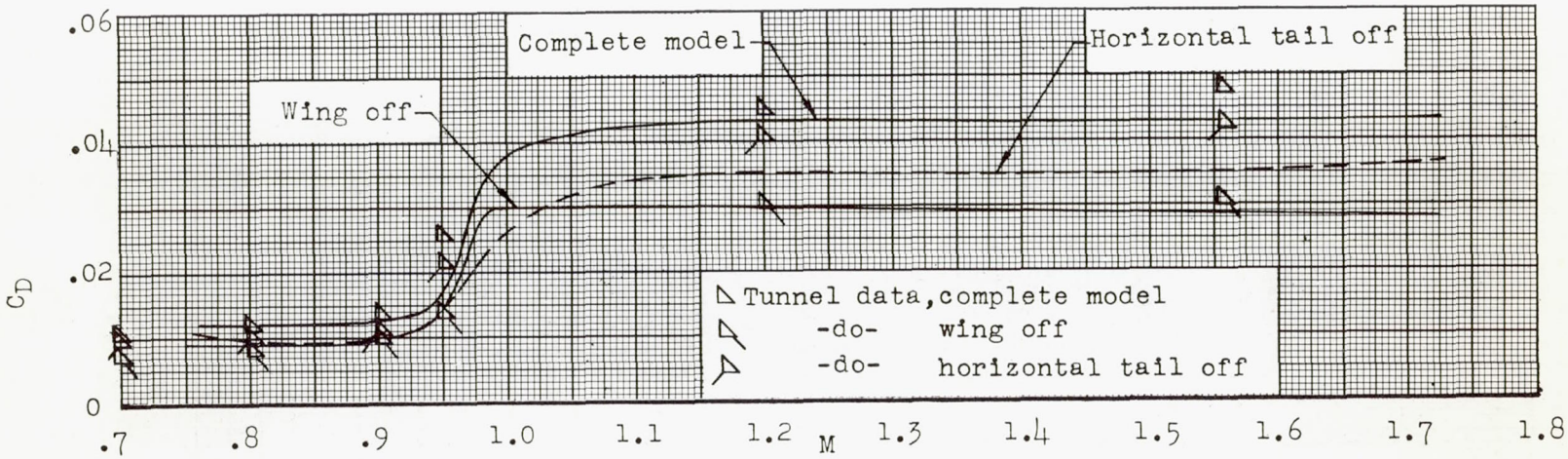

Figure 13.- Drag coefficient (first version), corrected to zero base drag.

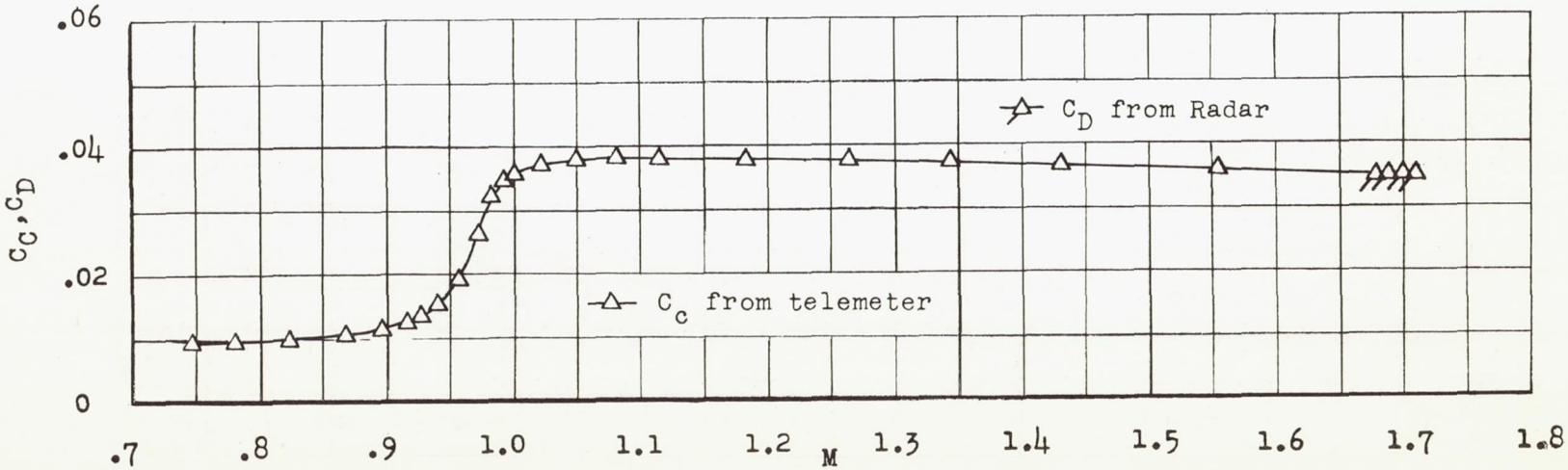

Figure 14.- Total drag and chord force (second version, complete model).

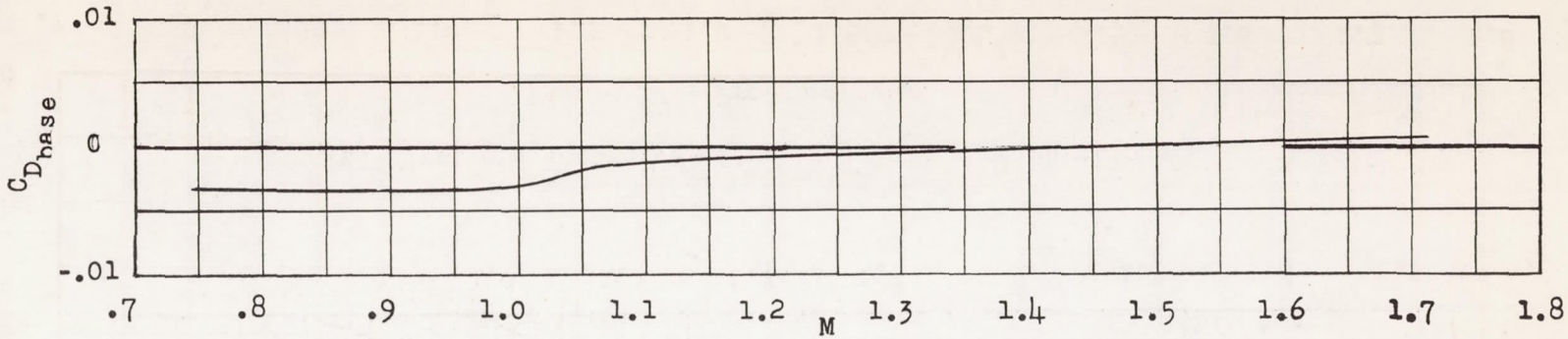

Figure 15.- Base drag (second version).

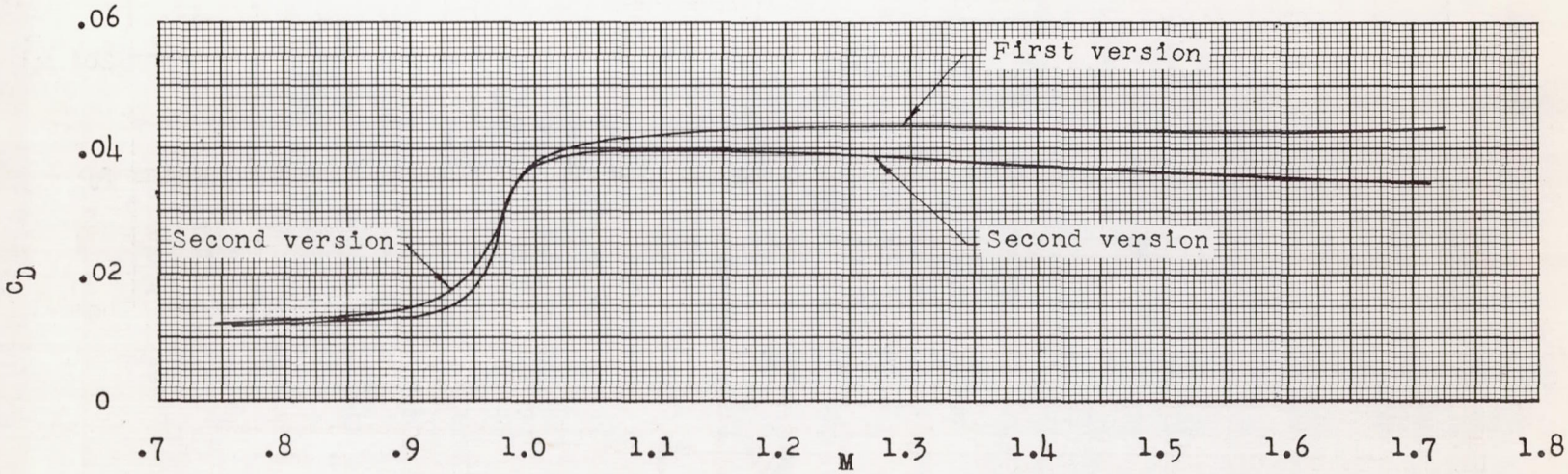

Figure 16.- Drag coefficient (complete models of both versions), corrected to zero base drag.

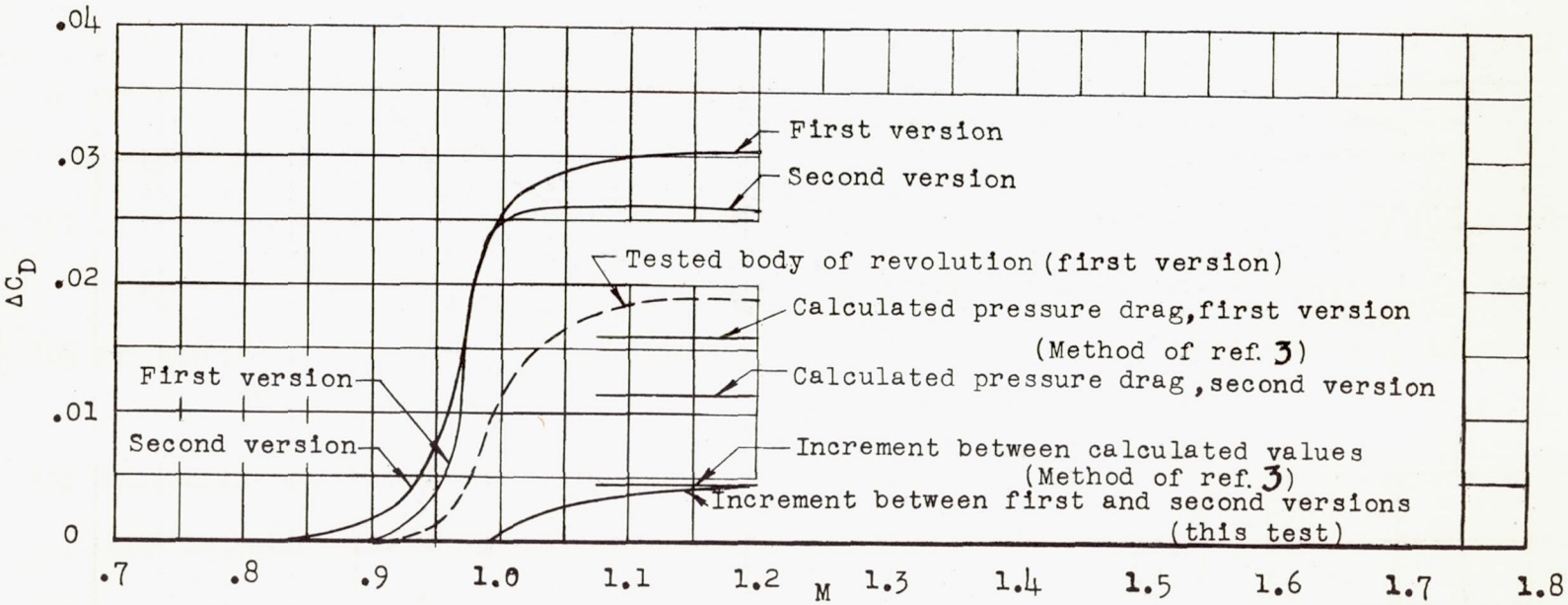

(a) First and second versions, complete configurations.

Figure 17.- Pressure drag.

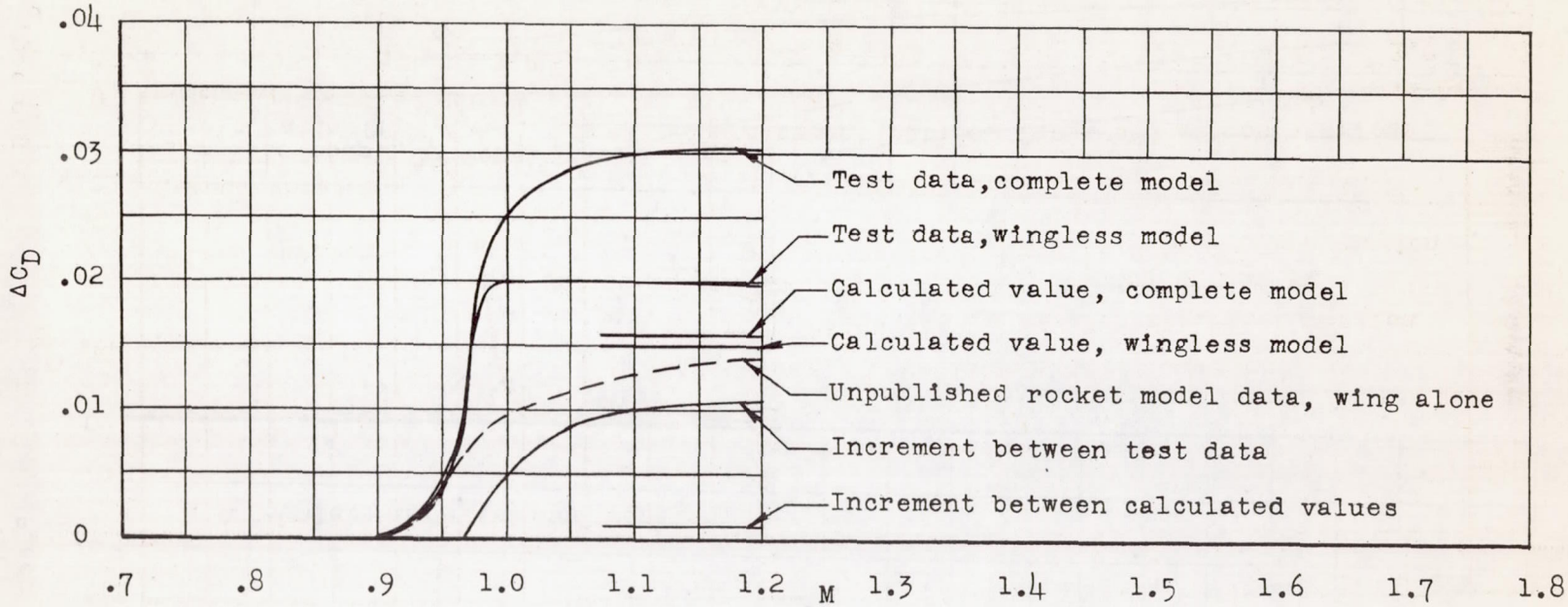

(b) First version, complete and wingless configurations.

Figure 17.- Concluded.

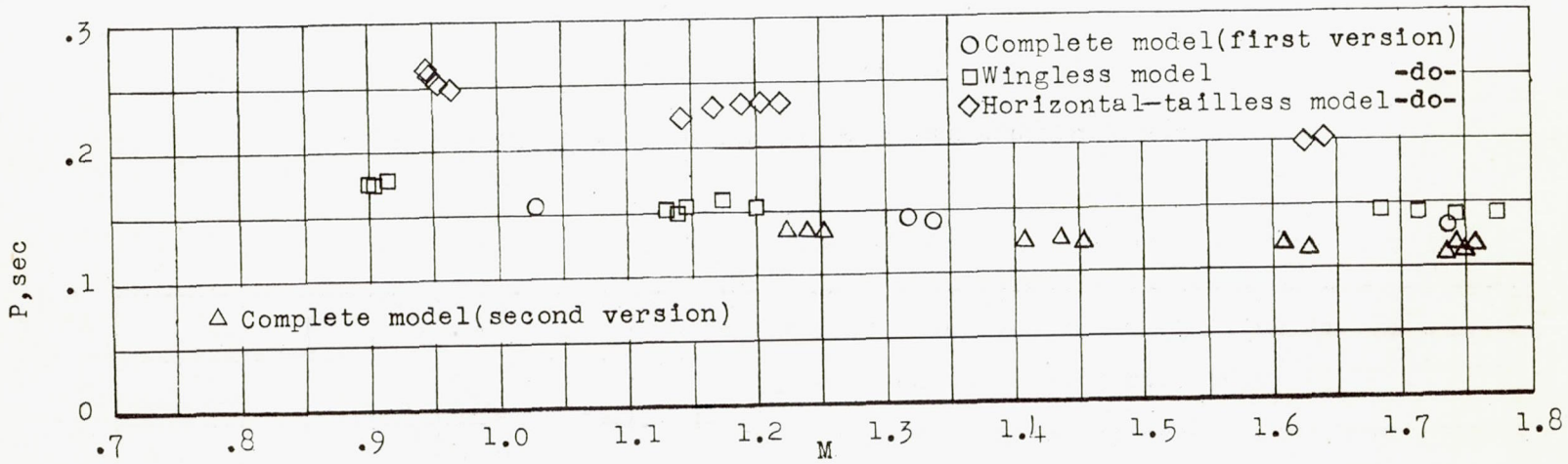

Figure 18.- Period of the short-period pitch oscillation.

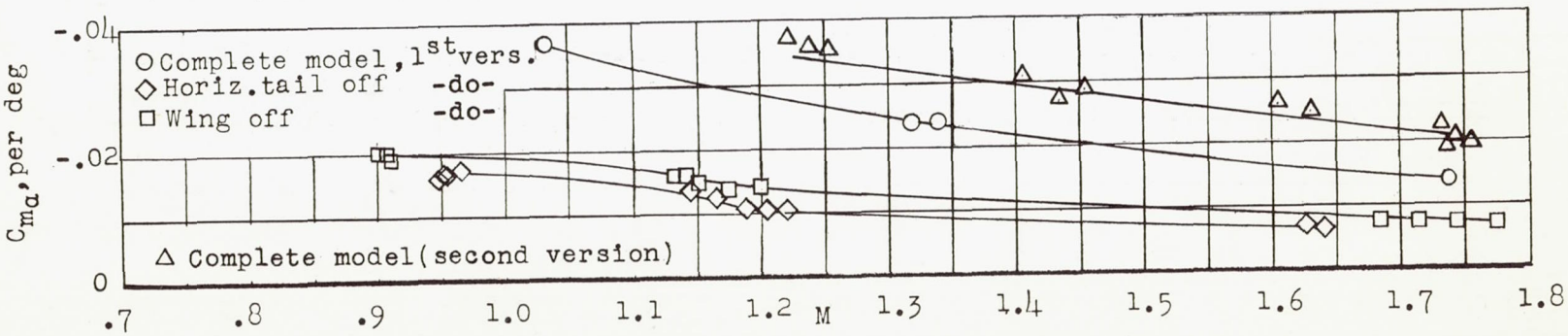

Figure 19.- Longitudinal stability parameter.

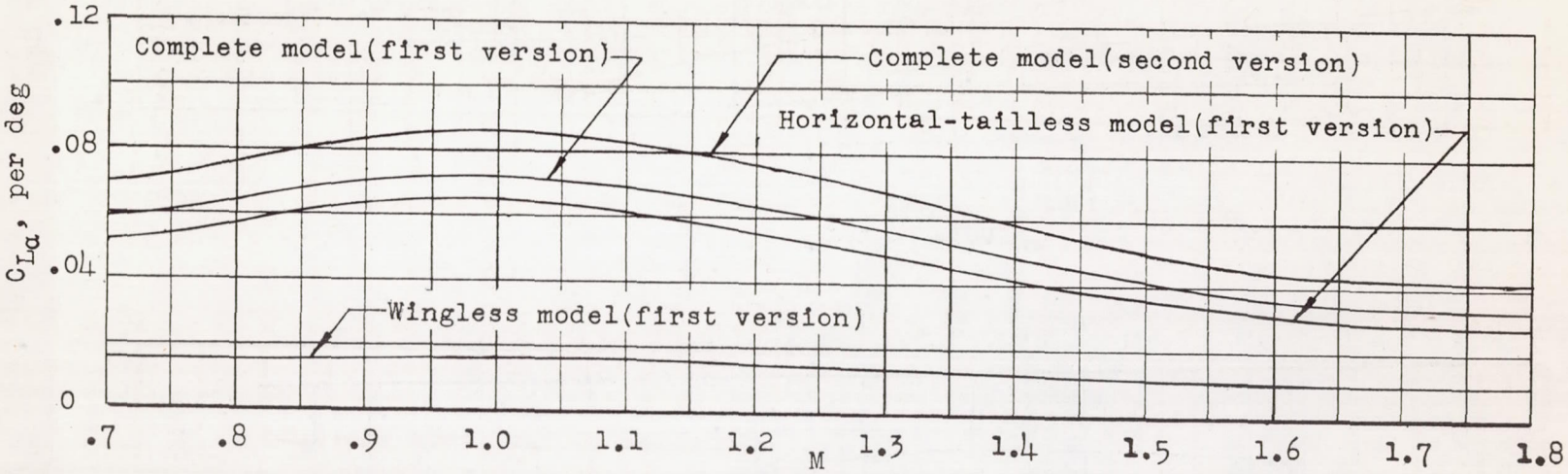

Figure 20.- Lift-curve slope from unpublished tunnel data, corrected for flexibility of the models tested.

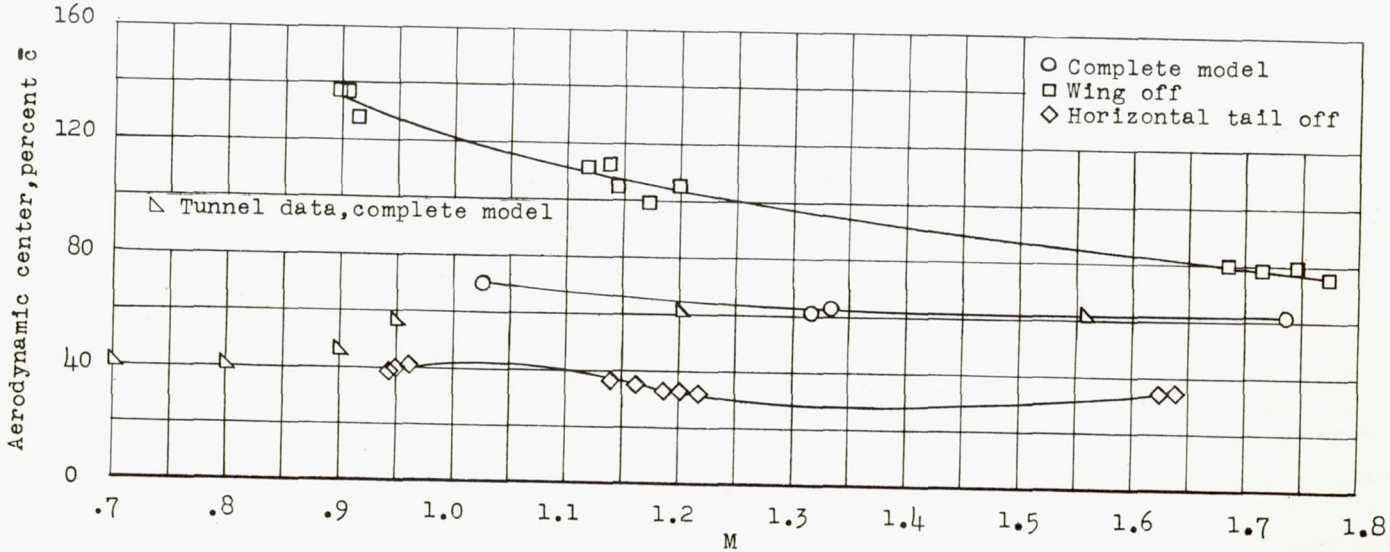

(a) The first version.

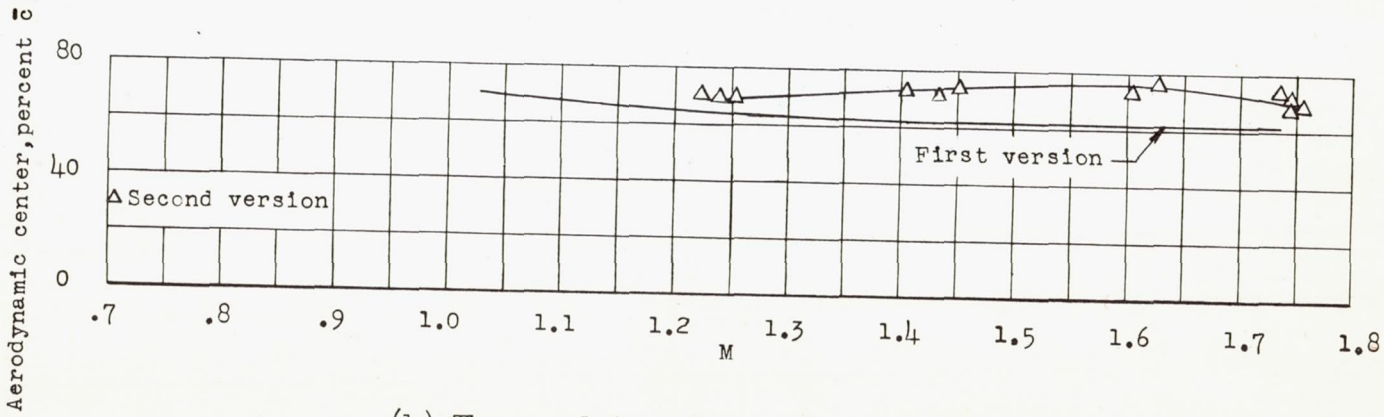

(b) The complete models of both versions.

Figure 21.- Aerodynamic-center location.

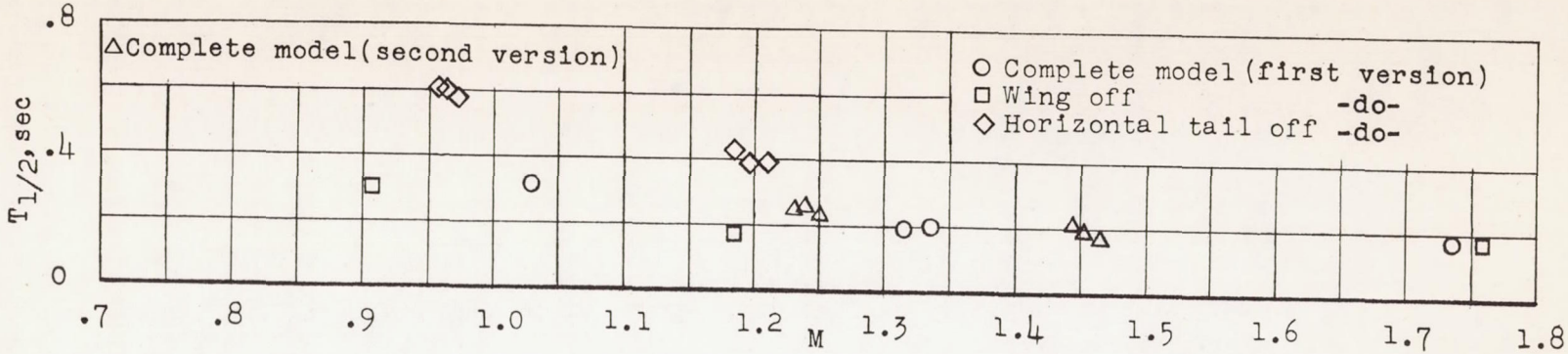

Figure 22.- Time required for the short-period pitch oscillation to damp to one-half amplitude.

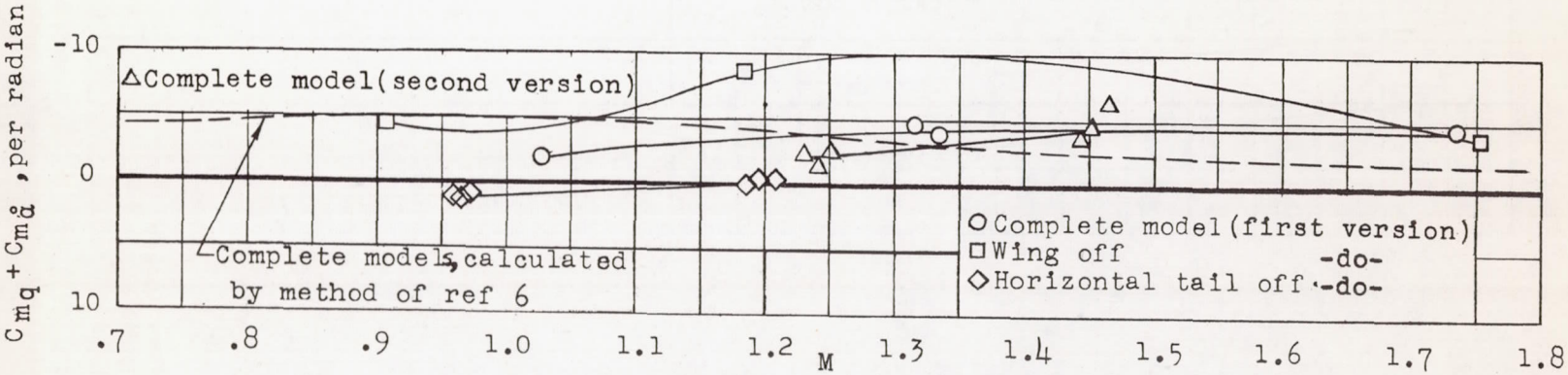

Figure 23.- Damping in pitch; center of gravity located 19.6, 8.8, and 16.7 percent behind the leading edge of the mean aerodynamic chord for the complete, wingless, and tailless models of the first version, respectively, and 20.6 percent for the complete model of the second version.

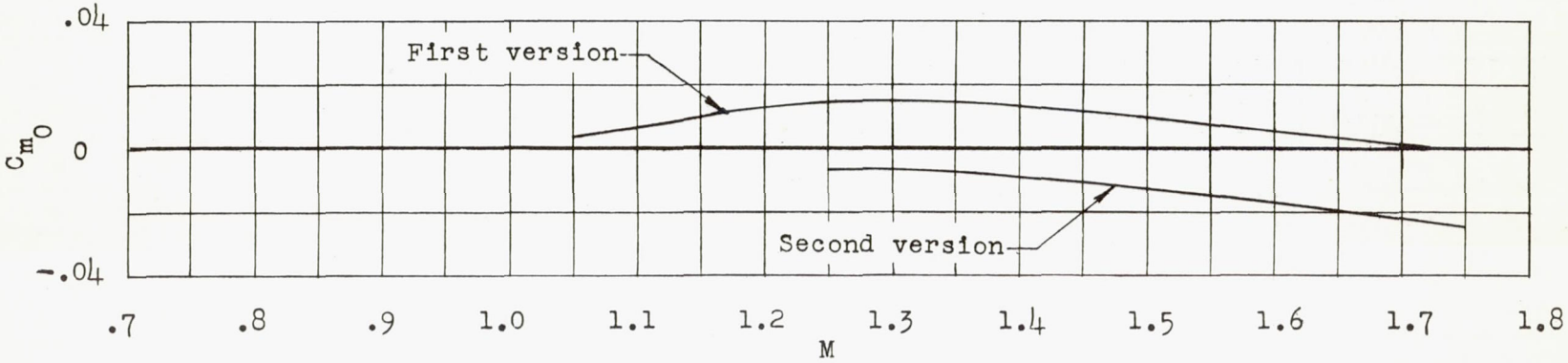

Figure 24.- Pitching-moment coefficient at zero lift for the complete models of both versions.

NACA-Langley - 11-26-54 - 300